The turbulent wake of a square prism with wavy faces

Y.F. Lin[1,4a], H.L. Bai[*2] and Md. Mahbub Alam[3b]

[1]*Shenzhen Key Laboratory of Urban Planning and Decision Making, Shenzhen Graduate School,
Harbin Institute of Technology, Shenzhen 518055, China*
[2]*Department of Civil and Environmental Engineering, Hong Kong University of Science and Technology,
Clear Water Bay, Kowloon, Hong Kong*
[3]*Shenzhen Graduate School, Harbin Institute of Technology, Shenzhen 518055, China*
[4]*Parsons Brinckerhoff (Asia) Ltd., Hong Kong*

Abstract. Aerodynamic effects, such as drag force and flow-induced vibration (FIV), on civil engineering structures can be minimized by optimally modifying the structure shape. This work investigates the turbulent wake of a square prism with its faces modified into a sinusoidal wave along the spanwise direction using three-dimensional large eddy simulation (LES) and particle image velocimetry (PIV) techniques at Reynolds number $Re_{Dm} = 16,500–22,000$, based on the nominal width (D_m) of the prism and free-stream velocity (U_∞). Two arrangements are considered: (i) the top and bottom faces of the prism are shaped into the sinusoidal waves (termed as WSP-A), and (ii) the front and rear faces are modified into the sinusoidal waves (WSP-B). The sinusoidal waves have a wavelength of $6D_m$ and an amplitude of $0.15D_m$. It has been found that the wavy faces lead to more three-dimensional free shear layers in the near wake than the flat faces (smooth square prism). As a result, the roll-up of shear layers is postponed. Furthermore, the near-wake vortical structures exhibit dominant periodic variations along the spanwise direction; the minimum (i.e., saddle) and maximum (i.e., node) cross-sections of the modified prisms have narrow and wide wakes, respectively. The wake recirculation bubble of the modified prism is wider and longer, compared with its smooth counterpart, thus resulting in a significant drag reduction and fluctuating lift suppression (up to 8.7% and 78.2%, respectively, for the case of WSP-A). Multiple dominant frequencies of vortex shedding, which are distinct from that of the smooth prism, are detected in the near wake of the wavy prisms. The present study may shed light on the understanding of the underlying physical mechanisms of FIV control, in terms of passive modification of the bluff-body shape.

Keywords: square prism; sinusoidal wavy face; passive control

1. Introduction

Turbulent flows around bluff bodies are tightly associated with aerodynamic forces and flow-induced vibration (FIV) of the structures, and thus are crucial in civil engineering applications such as high-rise buildings, cable-stayed bridges, and offshore struts. A slender square

---

∗Corresponding author, Ph.D., E-mail: hl_bai@126.com; hongleibai@ust.hk
[a] Email: mmyflin@gmail.com
[b] Professor, Email: alamm28@yahoo.com

prism is considered as one of the typical models of these bluff bodies. Boundary layers developing on the front face separate from the leading edges of the square prism, resulting in two free shear layers developing and rolling up into vortices in the near wake. Thus, geometric modification of the prism faces may alter the near wake flows and consequently reduce the aerodynamic forces and FIV (Choi *et al.* 2008). In a pioneering experimental work, Bearman and Owen (1998) found that a square prism with a sinusoidal front face could reduce time-averaged drag force by up to 30% compared with its smooth counterpart, at a Reynolds number $Re_{Dm} = 40,000$ based on the nominal width D_m of the prism and incoming free-stream velocity U_∞. The sinusoidal wave had a wavelength $\lambda = 6D_m$ and an amplitude $a = 0.25D_m$. Furthermore, vortex shedding from the prism was completely suppressed at a wave steepness $a/\lambda = 0.06$–0.09, suggesting suppression of fluctuating lift forces or FIV. At low $Re_{Dm} = 10$–150, Darekar and Sherwin (2001) numerically investigated the flow past a square prism with its both front and rear faces modified into sinusoidal waves ($\lambda/D_m = 1.0$–10.0 and $a/D_m < 0.75$). The two waves of the opposite faces had a 180° phase-shift, i.e., opposite variations of the two waves along the spanwise direction. Pairs of opposite-signed streamwise vorticity were identified along the spanwise direction in the near wake, with upwash and downwash flows induced by the streamwise vorticities at the locations of minimum and maximum protrusion to the incoming flow, respectively. A considerable reduction in the time-averaged drag (up to 16%) was achieved at $\lambda/D_m = 5.6$ and $a/D_m = 0.129$–0.168 ($Re_{Dm} = 100$), compared with a smooth square prism. However, one may wonder if the drag reduction could be further improved when the two waves of the front and rear faces are arranged in a 0° phase-shift? Recently, Lam *et al.* (2012) conducted a large eddy simulation (LES) on the flow past a square prism with its top and bottom faces modified into sinusoidal waves (in a 0° phase-shift) at $Re_{Dm} = 100$–$5,000$. A wavelength $\lambda/D_m = 6$ and an amplitude $a/D_m = 0.15$ were employed in their simulation. Significant reductions in drag (up to 12%) and fluctuating lift (up to 95%) were observed, which were ascribed to more three-dimensional and less unsteady shear layers of the wavy prism. Recently, New *et al.* (2013, 2015) investigated experimentally end-wall and confinement effects on the wake of wavy circular cylinders at $Re_{Dm} = 2,700$, but without aerodynamic forces examined. Nevertheless, it could be of interest to examine the turbulent wake of a square prism with wavy faces at a higher Reynolds number applicable to practical civil engineering applications.

This work aims to investigate the turbulent wake of a square prism with wavy faces, with a view to minimizing the aerodynamic effects such as drag force and FIV. Two arrangements are considered: (i) the top and bottom faces of the prism modified into sinusoidal waves (which is termed as WSP-A), and (ii) the front and rear faces modified into sinusoidal waves (WSP-B). The sinusoidal wave has a wavelength $\lambda = 6D_m$ and an amplitude $a = 0.15D_m$, similarly to Lam *et al.* (2012). Investigations are conducted at higher $Re_{Dm} = 16,500$–$22,000$ than in the literature, using three-dimensional LES and particle image velocimetry (PIV) techniques. Sections 2 and 3 describe the computational models and numerical simulation details, respectively, followed by experimental details in section 4. Results are presented and discussed in section 5. This work is concluded in section 6.

2. Square prism models

Fig. 1 presents computational models of the two wavy square prisms considered in this study. While Fig. 1(a) illustrates the wavy square prism A (i.e., WSP-A) where the top and bottom faces

are modified into sinusoidal waves, Fig. 1(b) shows the wavy square prism B (WSP-B) where the front and rear surfaces are modified into sinusoidal waves. The prism geometry is described by the following Eq. (1), viz.,

$$D(z) = D_m + 2a \cos(2\pi z / \lambda) \tag{1}$$

where $D(z)$ is the local width (or height) of the wavy prism and varies sinusoidally along the spanwise z direction. D_m [= $(D_{min} + D_{max})/2$] is the nominal width (Fig. 1(a)) or height (Fig. 1(b)) of the prism, where D_{min} and D_{max} denote the minimum (i.e., saddle) and maximum (i.e., nodal) width (or height) of the prism, respectively. Presently, one wavelength $\lambda = 6D_m$ with a fixed wave amplitude $a = 0.15D_m$ is considered (Table 1); this value of the wavelength for a circular case rendered an optimum performance to reduce drag and fluctuating lift (Lam and Lin 2009, Lam *et al*. 2010). A smooth square prism (SSP) with the nominal width D_m is taken as the baseline. The streamwise and cross-stream directions are designated as x and y, respectively.

3. Numerical simulation

3.1 Governing equations

A three-dimensional LES is carried out in the present work at a subcritical $Re_{Dm} = 22,000$. The Fluent software-based finite volume method with an unstructured hexahedral grid is employed to solve the unsteady incompressible Navier-Stokes (NS) equations. Governing equations adopted in the LES are as follows
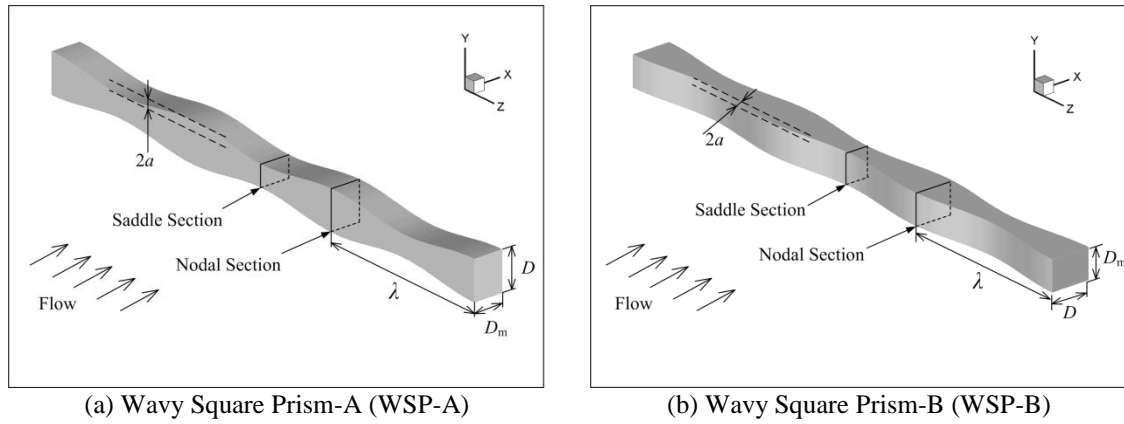

(a) Wavy Square Prism-A (WSP-A)   (b) Wavy Square Prism-B (WSP-B)

Fig. 1 Computational models of the wavy square prisms

Table 1 Computational models

Model	a/D_m	λ/D_m	L_z/D_m	Δt^*	Cells
SSP	-	-	6	0.01	280×180×120
WSP-A	0.15	6	6	0.01	280×180×120
WSP-B	0.15	6	6	0.01	280×180×120

$$\frac{\partial \overline{u}_i}{\partial x_i} = 0 \tag{2}$$

$$\frac{\partial \overline{u}_i}{\partial t} + \frac{\partial \overline{u}_i \overline{u}_j}{\partial x_j} = -\frac{1}{\rho}\frac{\partial \overline{p}}{\partial x_i} + \nu \frac{\partial^2 \overline{u}_i}{\partial x_j \partial x_j} - \frac{\partial \tau_{ij}}{\partial x_j}, \quad (i, j = 1, 2, 3) \tag{3}$$

where $\overline{u}_i$ are the filtered velocity components along the Cartesian coordinates x_i (x_1, x_2 and x_3 corresponding to x, y and z directions, respectively), $\overline{p}$ is fluid pressure, ρ fluid density, υ kinematic viscosity of the fluid, and τ_{ij} denotes subgrid-scale stresses. Large-scale eddies are directly solved by the filtered NS equations, whilst small-scale eddies are modeled via the well-known Smagorinsky model (1963) (i.e., $\tau_{ij} = \overline{u_i u_j} - \overline{u}_i \overline{u}_j$). The Smagorinsky constant $C_s = 0.1$ in all the present computations, based on Liang and Papadakis (2007) and Lam *et al.* (2012). A second-order central difference scheme is adopted for momentum discretization while a second-order implicit scheme for temporal discretization. Moreover, the well-known pressure implicit method with splitting of operators (PISO) algorithm is used to deal with the pressure-velocity coupling between the momentum and the continuity equations. More detailed descriptions and validation tests of the present LES method for turbulent flows around bluff bodies can be found in Lam and Lin (2008) and Lam *et al.* (2010, 2012).

3.2 Computational domain and boundary conditions

The computational domain ($L_x \times L_y \times L_z$) is set to be $L_x = 24D_m$, $L_y = 16D_m$ and $L_z = \lambda = 6D_m$ along the streamwise, cross-stream and spanwise directions, respectively (Fig. 2). The prism is located in the middle of the cross-stream domain. The upstream and downstream boundaries are at $8D_m$ and $16D_m$ away from the prism center, respectively. Similar sizes of the computational domain were adopted by Lam *et al.* (2010, 2012) for the turbulent wake of a sinusoidal wavy circular cylinder and by Noda and Nakayama (2003), Sohankar (2008), Kuroda *et al.* (2007) and Bruno *et al.* (2010) for the turbulent wake of a rectangular cylinder. The spanwise computational size $L_z = \lambda = 6D_m$ is sufficient in the simulation of the turbulent wake of a square prism. For example, $L_z = 5D_m$ was chosen by Mannini *et al.* (2010) and Mankbadi and Georgiadis (2015) and their simulations captured the large scale streamwise vortices in the near wake. However, validation tests are carried out in the present work by extending L_z to 2λ ($= 12D_m$) for several typical cases. No significant changes are observed in the near-wake structures and the force values.

Uniform incoming velocity is set at the inlet boundary, while the Newmann-type boundary condition at the outlet boundary. Periodic boundary condition is employed in the spanwise z direction or, in other words, the prism model is considered as an infinitely long one; as such, the end wall effect is avoided. No-slip boundary condition (i.e., $u_i = 0$) is used at the prism surfaces, whereas the lateral faces are treated as slip surfaces using symmetry boundary conditions. Similar boundary conditions were employed by Oka and Ishihara (2009) for the turbulent flow past a smooth square cylinder and by Sohankar (2008) for smooth rectangular cylinders.

As shown in Fig. 2, the computational domain is divided into a number of unstructured hexahedral grids, which are non-uniform in the xy plane and uniform along the spanwise z direction. The grids are clustered near the prism surface so as to resolve the viscous sublayer of the

near-wall region corresponding to a distance of $y^+ \leq 1$ between the prism surface and the nearest grid points (Lam *et al.* 2010, 2012). Away from the prism surface, the mesh spacing is properly increased at a ratio of 1.1 (e.g., Lam *et al.* 2012). A non-dimensional time step $\Delta t^* = \Delta t U_\infty / D_m = 0.01$ is chosen in the simulation, yielding sufficiently small Courant-Friedrichs-Lewy (CFL) number of < 1 for the most part of the computational domain. A computing time of > $1,500 \Delta t^*$, which corresponds to about 15 cycles of vortex shedding in the near wake, is conducted for each case of the simulation, ensuring statistically convergent results.
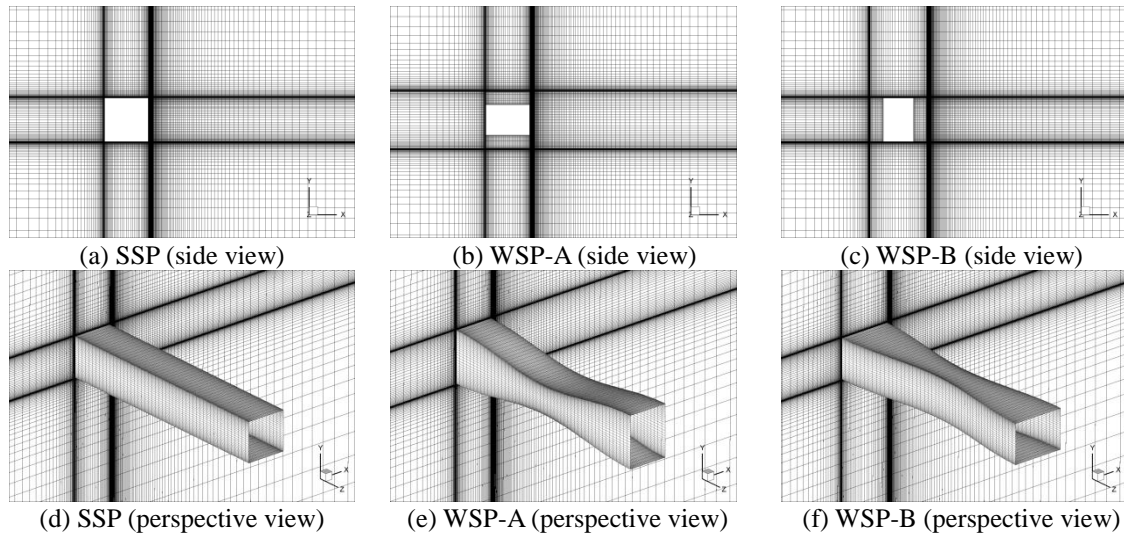

| (a) SSP (side view) | (b) WSP-A (side view) | (c) WSP-B (side view) |
| (d) SSP (perspective view) | (e) WSP-A (perspective view) | (f) WSP-B (perspective view) |

Fig. 2 Computational grids of the smooth and wavy square prisms

Table 2 Tests of grid independence for a smooth square prism

Test		Re_{Dm}	Δt^*	Cells	$\overline{C}_D$	C'_L	St
I	LES	22000	0.01	$240 \times 140 \times 80$	2.13	1.08	0.127
II	LES	22000	0.01	$280 \times 180 \times 120$	2.16	1.21	0.132
III	LES	22000	0.005	$280 \times 180 \times 120$	2.17	1.25	0.134
Sohankar *et al.* 2000	LES-SSM	22000	0.025	$185 \times 105 \times 25$	2.22	1.50	0.127
Lo *et al.* 2005	LES-D2-LS	22000	-	-	2.18	-	0.134
Norberg 1993	Exp.	13000	-	-	2.11	-	0.131
Norberg 1993	Exp.	22000	-	-	2.10	-	0.130
Lyn *et al.* 1995	Exp.	21400	-	-	2.10	-	0.130

3.3 Grid-independence tests

Grid-independence tests are performed for a smooth square prism. Table 2 lists the detailed information. Three tests of different computational cells and time steps are carried out and compared with each other as well as with data from the literature. Coefficients of time-averaged drag and fluctuating lift are defined by $\overline{C}_D = 2\overline{F}_D \big/ \rho U_\infty^2 D_m \lambda$ and $C_L' = 2F_L' \big/ \rho U_\infty^2 D_m \lambda$, respectively, where F_D and F_L are the drag and lift forces acting on a length of λ of the square prism, respectively, and 'overbar' and 'prime' denote time-averaged and root-mean-square (*rms*) values, respectively. In general, $\overline{C}_D$ and C_L', and Strouhal number *St* computed presently are in good agreements with those from the literature. The maximum deviations of the present $\overline{C}_D$ and *St* (test III) from the experimental results (Norberg 1993, $Re_{Dm} = 22{,}000$; Lyn *et al*. 1995, $Re_{Dm} = 21{,}400$) are only about 3%. As the computational cells are increased from $240 \times 140 \times 80$ (test I) to $280 \times 180 \times 120$ (tests II & III), $\overline{C}_D$ and *St* vary less than 1.5% and 4%, respectively. When the time step Δt^* is reduced from 0.01 (test II) to 0.005 (test III), $\overline{C}_D$, C_L' and *St* are only changed by about 1%, 3% and 2%, respectively. Therefore, the computational cells ($280 \times 180 \times 120$) and time step $\Delta t^* = 0.01$ in test II are adopted for all the computations of both the smooth and wavy square prisms. Moreover, the computational results are compared with experimental measurements, which will be discussed in section 5, thus providing further validation.

4. PIV measurements

To validate and supplement the numerical data, PIV technique is employed to measure the flow field in the near wakes of the smooth and wavy square prisms in a closed-circuit water tunnel with a working section of 0.3 m × 0.6 m (width × height) in cross-section and 2.4 m in length. See more details of the tunnel in Lam *et al*. (2010, 2012). The square prism models, made of aluminum, are placed horizontally at the midsection of the tunnel. The prism models are of a nominal width $D_m = 1.5$ cm and span the entire tunnel width, yielding a blockage of 5%. The incoming flow has a free-stream velocity $U_\infty = 1.1$ m/s, corresponding to $Re_{Dm} = 16{,}500$, slightly different from that ($Re_{Dm} = 22{,}000$) in the LES. Given both Reynolds numbers are in the subcritical Reynolds number regime, the flow structures at the two Reynolds numbers should render similar behaviours (Gu and Sun 1999).

A Dantec standard PIV system is deployed to measure spanwise vorticity and velocity distributions in the cross-stream plane (i.e., *xy* plane) of different spanwise locations. The flow is seeded by polyamide particles of 20 μm diameter, with a density of 1.03 g/cm^3. Two overlapped light sheets of Nd: YAG pulsed laser, each having a wavelength of 532 nm and the maximum energy of 120 mJ, are used to illuminate the concerned flow fields of $6D_m \times 6D_m$. A frame-straddle CCD camera (Hisense, 1024 × 1024 pixels) is used for image capture. Velocity vectors are calculated, based on spatial cross-correlation algorithm, using a Dantec Flow Map Process (type PIV2001), with an interrogation window size of 32 × 32 pixels and 50% overlapping in both directions, producing 3,969 vectors and the same number of vorticity data. A total of 150 PIV image pairs are obtained for each measurement. More information on the PIV system can be found in Lam *et al*. (2004).

5. Results and discussion

5.1 Force characteristics

Fig. 3 presents time histories of the drag and lift coefficients for both smooth and wavy square prisms at $Re_{Dm} = 22,000$. The force coefficients become steady at the time $t^* = tU_\infty/D_m > 20$, indicating a convergence of the computation. For the smooth square prism (SSP, Fig. 3(a)), the lift coefficient C_L exhibits a great oscillation, which is associated with the alternating vortex shedding in the near wake. The oscillation magnitude of C_L is even greater than 2. Periodicity is also discernible in the drag coefficient C_D in Fig. 3(a). On the other hand, there are remarkable changes in the behaviors of C_D and C_L for the wavy square prisms (WSP-A and B, Figs. 3(b) and 3(c), respectively). The oscillation magnitudes of C_D and C_L are significantly reduced, in particular for WSP-A, suggesting a greater suppression of the fluctuating lift or FIV. The comparison of force coefficients between the smooth and wavy square prisms is provided in Table 3. $\overline{C}_D$ is reduced by 8.7% and 2.4% for WSP-A and WSP-B, respectively, compared with that of SSP. The reduction is more significant in C_L' than in $\overline{C}_D$; up to 78.2% and 32.1% reductions in C_L' are obtained for WSP-A and WSP-B, respectively. This observation indicates that WSP-A produces a more stabilized near-wake than WSP-B.
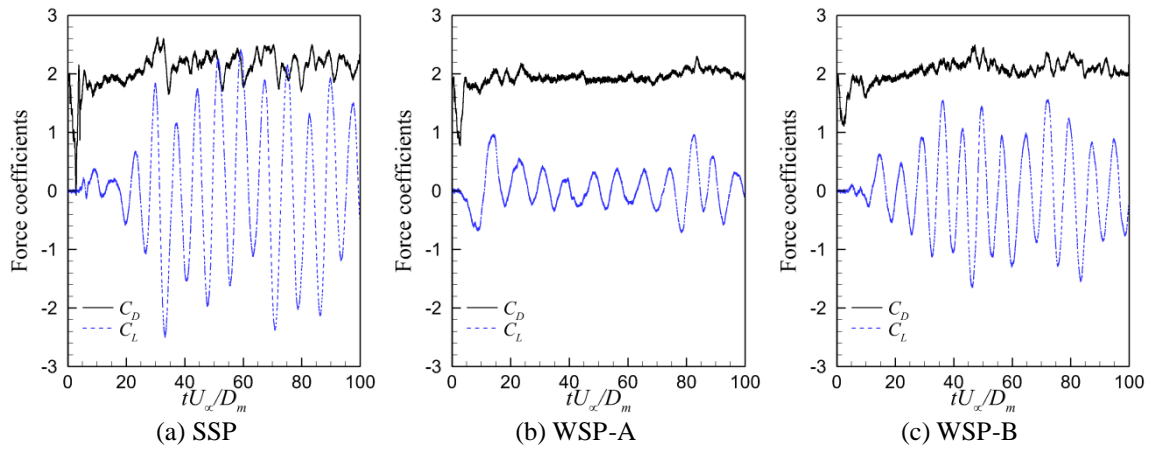

Fig. 3 Time histories of drag (C_D) and lift force (C_L) coefficients of the smooth and wavy square prisms. SSP: smooth square prism; WSP-A: wavy square prism A; WSP-B: wavy square prism B. $Re_{Dm} = 22,000$

Table 3 Comparison of force coefficients between smooth and wavy square prisms at $Re_{Dm} = 22,000$

Model	a/D_m	λ/D_m	$\overline{C}_D$	%	C_L'	%	St
SSP	-	-	2.16	(0)	1.21	(0)	0.132
WSP-A	0.15	6	1.97	(-8.7)	0.26	(-78.2)	0.121
WSP-B	0.15	6	2.10	(-2.4)	0.82	(-32.1)	0.142

Power spectra of the fluctuating lift are examined for WSP-A, -B, and SSP (Fig. 4), based on the fast Fourier transform of the time histories of the fluctuating lift. The abscissa denotes normalized frequency $f^* = fU_\infty/D_m$, where f is the Fourier frequency. Obviously, there is a pronounced peak in the spectrum, which is associated the dominant vortex-shedding frequency in the near wake. The peak occurs at $f^* = 0.132$ for SSP, close to the experimental result by Norberg (1993). However, the peaks for WSP-A and -B are detected at $f^* = 0.121$ and 0.142, lower and higher than that for SSP, respectively. This observation suggests a dominant vortex-shedding frequency, different from that of SSP, appearing in the near wake of the wavy square prisms. Further, it can be seen that the power spectrum for WSP-A is weaker than that for WSP-B and also SSP, given the same scales employed in the vertical axes of Fig. 4, echoing the greatly suppressed fluctuating lift observed (Fig. 3 and Table 3).

5.2 Near-wake flow patterns

Typical flow structures in the near wakes of the wavy square prisms are presented in Figs. 5 and 6, in terms of spanwise vorticity (ω_z) distributions. The case of the smooth square prism is also provided for comparison. Evidently, the large-scale near-wake flow structures are captured by the LES, qualitatively consistent with those from the PIV measurement. It can be seen that, for both smooth and wavy square prisms, flow separation occurs (and is fixed) at the upper and lower leading edges, which is distinct from the circular cylinder case where flow separation is instead oscillatory on the leading surface. In general, the separated shear layers overshoot the prism and roll up into staggered vortices in the near wake. However, the vortical structures in the near wake of the wavy square prisms behave distinctly from those of the smooth square prism, as discussed below.

Firstly, for WSP-A (Figs. 5(b) and 5(d), Figs. 6(b) and 6(d)), there are wide and narrow wakes behind the node and saddle locations, respectively. The sinusoidal waves of the top and bottom faces impose the maximum protrusion to the incoming flow at the node location (Figs. 5(b) and 6(b)), where the width-to-height ratio of the prism is $1/1.3 = 0.77$, thus generating the wide wake behind. On the other hand, the cross-section of the prism at the saddle location (Figs. 5(d) and 6(d)) is rectangular having a longitudinal extension, with a width-to-height ratio of $1/0.7 = 1.43$, which elongates the shear layers before their rolling-up into vortices in the near wake. These observations, consistent with that by Lam *et al.* (2012, $Re_{Dm} = 100-5,000$), indicate that WSP-A has a more three-dimensional near-wake than SSP, due to the modification of the top and bottom faces. Further, the near wake of WSP-A, particularly behind the saddle, seems more stable than that of SSP, internally connected with the reductions in drag and fluctuating lift.

Secondly, for WSP-B (Figs. 5(c) and 5(e), Figs. 6(c) and 6(e)), narrow and wide wakes are produced behind the node and saddle locations, respectively, which is opposite to that for WSP-A. Sinusoidal waves are employed on the front and rear faces of WSP-B. The node location (Figs. 5(c) and 6(c)) has the maximum longitudinal extension (with a width-to-height ratio of 1.3), which may delay the shear layer development and elongate the near-wake recirculation bubble; on the other hand, the saddle location (Figs. 5(e) and 6(e)) has the maximum cross-stream extension or protrusion (with a width-to-height ratio of 0.7), resulting in the wide wake. Similarly to the observation in the saddle of WSP-A, the narrow wake behind the node of WSP-B also seems more stable than that behind SSP, again corroborating the drag and fluctuating lift reductions.
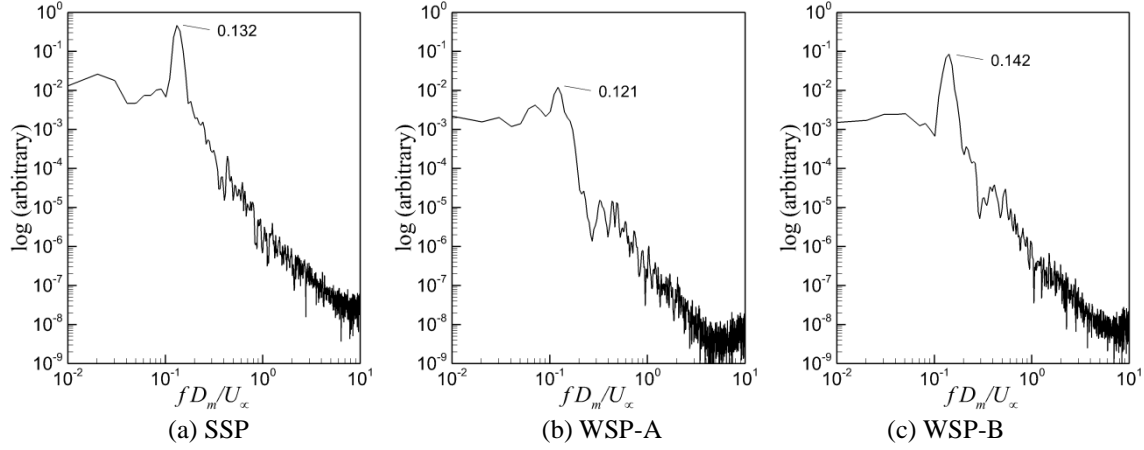
Fig. 4 Power spectra of the fluctuating lift for the smooth and wavy square prisms. SSP: smooth square prism; WSP-A: wavy square prism A; WSP-B: wavy square prism B. Re_{Dm} = 22,000
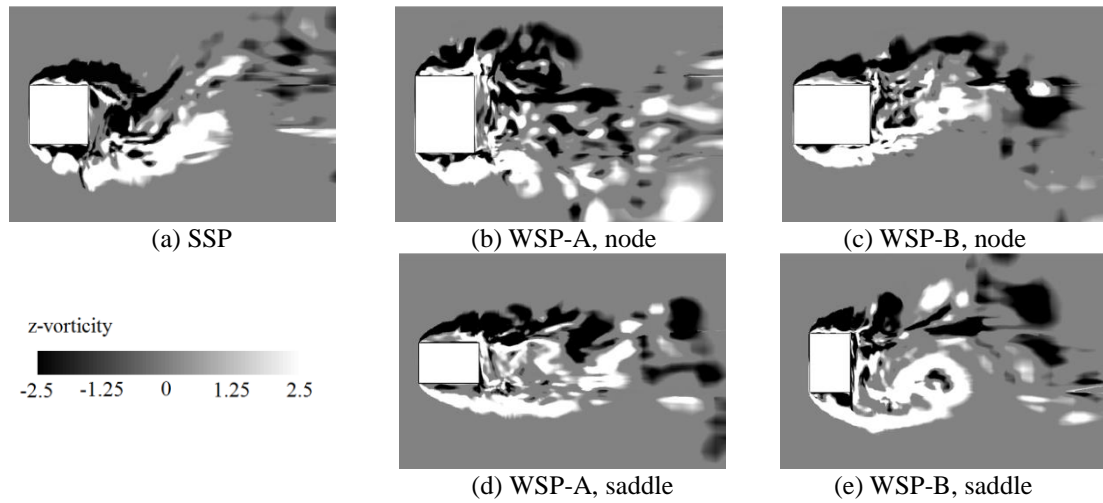

Fig. 5 Typical instantaneous spanwise vorticity ($\omega_z^* = \omega_z D_m/U_\infty$) in the near wakes of the smooth and wavy square prisms from the LES. The white and dark grey indicate the positive and negative ω_z^*, respectively. Re_{Dm}=22,000

Thirdly, the vortex formation length at the saddle of WSP-A is longer than that at the node of WSP-B, which is partially ascribed to the larger width-to-height ratio (1.43) of the former than that (1.3) of the latter and partially to the more stabilized shear layers of the former. At the node of WSP-B (Fig. 5(c)) the shear layers reattachments upon the top and bottom faces are identified based on the visual examination of the instantaneous flow structures. The occurrence of the reattachments may impair the vortices development and lead to instability in the near wake.
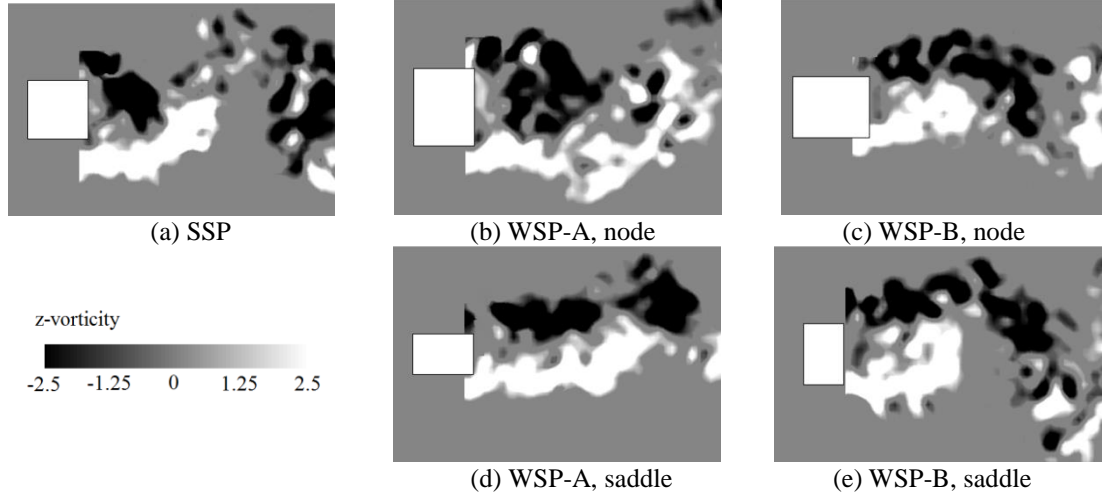
Fig. 6 Typical instantaneous spanwise vorticity ($\omega_z^* = \omega_z D_m/U_\infty$) in the near wakes of the smooth and wavy square prisms from the PIV measurement. The white and dark grey indicate the positive and negative ω_z^*, respectively. Re_{Dm}=16,500
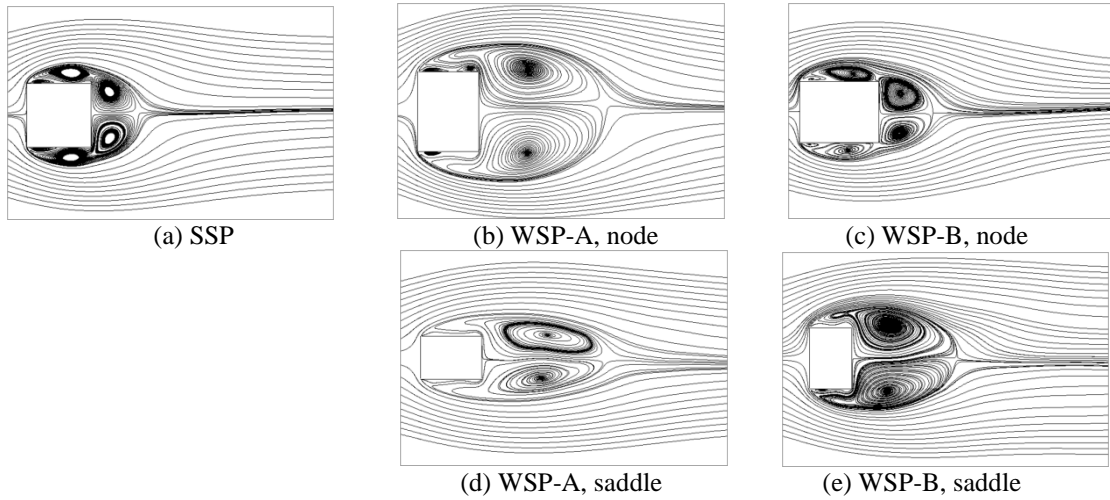

Fig. 7 Time-averaged streamlines in the *xy*-plane in the near wakes of the smooth and wavy square prisms from LES. Re_{Dm}=22,000

Time-averaged streamline patterns around the smooth and wavy square prisms from the LES are presented in Fig. 7. For the smooth square prism, a pair of counter-rotating reversed flow regions is identified immediately in the base region. The topologic saddle point in the streamline pattern, where the streamlines bifurcate and the streamwise velocity is zero, is about $1.3D_m$ away from the prism center. Reversed flows also occur on the sides of the prism. For the wavy square

prisms, it can be seen that the reversed flow regions in the base are wider and longer than those for the smooth square prism, suggesting an elongated recirculation bubble in the near wake and recovered base pressure (or reduced drag force). Furthermore, WSP-A has the widest and longest reversed flow region in the near wake (Figs. 7(b) and 7(d)), corroborating the greatest reduction in drag (Table 3).

The time-averaged streamline patterns in the xz-plane at the wake center ($y = 0$) of the wavy square prisms (Fig. 8) are examined, to deepen our understanding of the three-dimensional near wakes and also uncover the underlying mechanisms of drag reduction. The smooth square prism case (Fig. 8(a)) is also provided for comparison. Similarly to that in the xy-plane, the bifurcation location of the streamlines in the base region indicates the streamwise length of the recirculation bubble or the vortex formation length. For SSP, the bifurcation occurs mostly at the same location (i.e., about $1.3D_m$ downstream of the prism center) along the spanwise direction. However, the bifurcation locations for WSP-A and -B exhibit distinct features from that for SSP. Firstly, the bifurcation locations for WSP are further downstream than that for SSP, which are internally associated with the elongated recirculation bubbles and the reduced forces. The spanwise-averaged bifurcation locations of the streamlines are about $2.5D_m$ and $2D_m$ downstream of the prism center for WSP-A and -B, respectively. Secondly, there is a great variation of the bifurcation locations for the wavy square prisms, particularly for WSP-B. For WSP-A, the bifurcation location is relatively recessed in the middle part (i.e., downstream of the saddle), indicating the retreated recirculation bubble length. For WSP-B, the bifurcation location is relatively elevated in the middle part (i.e., downstream of the saddle), indicating the elongated recirculation bubble length. These observations of the streamline patterns are consistent with those of the force behaviors; further, they may imply that the node section of WSP-A and the saddle section of WSP-B are more capable of reducing the forces. Interestingly, New *et al.* (2013) found that there was a significant difference of vortex formation length when the wavy circular cylinders were arranged in a node- and saddle-configuration, with the former generated a relatively longer spanwise-averaged vortex formation length; however, the recessed and elongated vortex formation length were produced downstream of the node and saddle, respectively, for $\lambda/D_m = 2.0$ and $a/D_m \geq 0.2$, regardless of the node- or saddle-configuration arrangement (see their Fig. 19). Thirdly, the three-dimensional near wakes of WSP are featured by the streamline patterns. For SSP, the streamlines both inside and outside of the recirculation bubble are roughly parallel to the freestream flow or, in other words, normal to the spanwise direction. However, for the wavy square prisms, the streamlines are heading to the middle part (i.e., the saddle section), implying the spanwise components of the near-wake flows generated due to the modification of the prism faces.

Moreover, typical three-dimensional flow structures in the near wakes of the wavy and smooth square prisms are presented in Fig. 9, in terms of iso-surfaces of the streamwise velocity detected based on a Q-criterion (Hunt *et al.* 1998). A threshold (i.e., Q = 1,500,000) is set on the second invariant of the velocity gradient tensor to visualize the coherent structures in the near wake. For SSP (Figs. 9(a) and 9(d)), the iso-surfaces display a staggered pattern in the near wake, in line with the well-known Karman vortex street. However, different flow characteristics are observed for WSP. For WSP-A, the arrangement of the iso-surfaces in the near wake is less staggered; the coherent structures are more stable than those for SSP, corresponding to the elongated recirculation bubble or vortex formation length (Figs. 7 and 8). For WSP-B, the iso-surfaces appear staggered in the near wake, similarly to those for SSP. However, larger coherent structures connected to the wavy faces of the prism (Fig. 9(f)) are identified in the near wake of the former, contributing to the increased size of the recirculation bubble (Figs. 7 and 8). Compared with the

SSP case, the near wakes of WSP are more coherent along the spanwise direction, which is ascribed to the face modification of the prism and the consequent narrow and wide wakes.
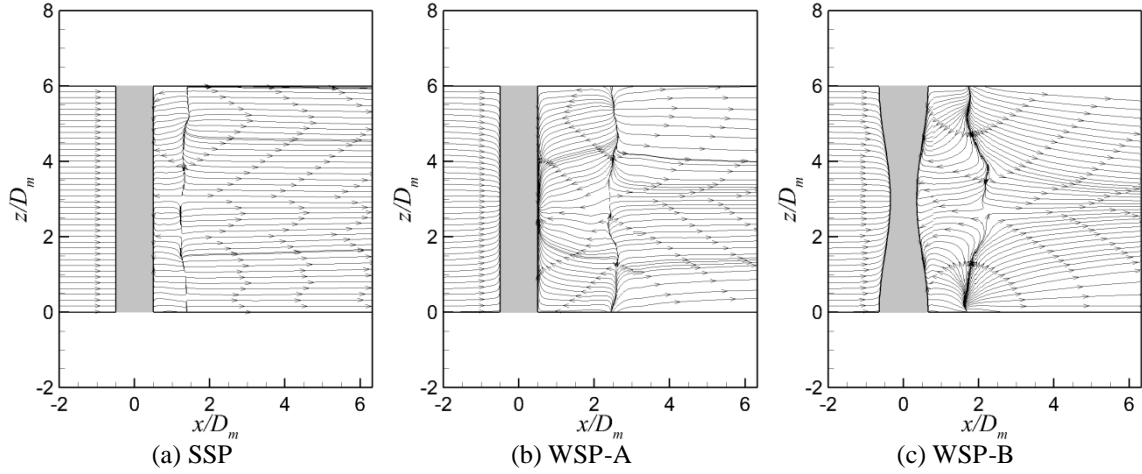

(a) SSP   (b) WSP-A   (c) WSP-B

Fig. 8 Time-averaged streamlines in the *xz*-plane at the wake centerline ($y = 0$) of the smooth and wavy square prisms. Arrow heads are added to the streamlines to indicate the flow direction
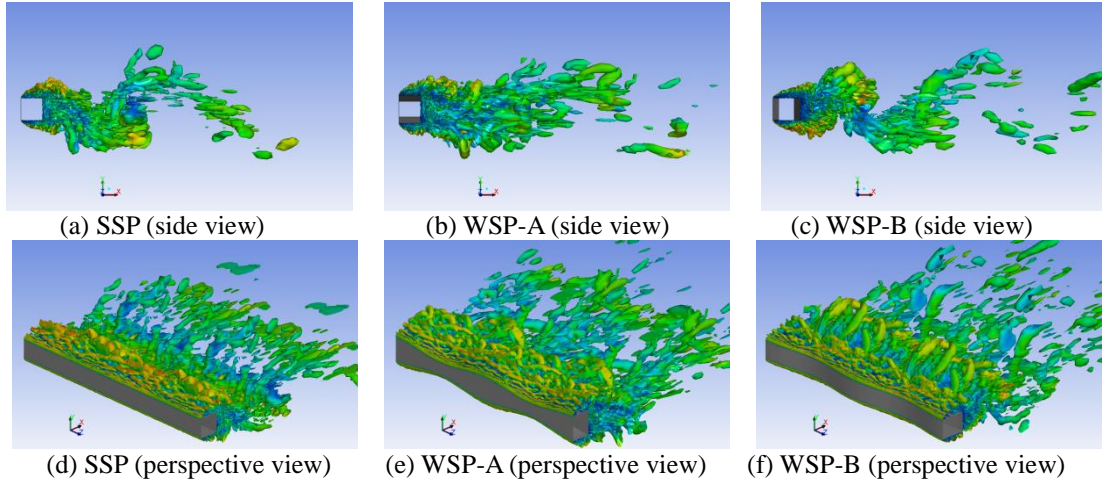

(a) SSP (side view)   (b) WSP-A (side view)   (c) WSP-B (side view)

(d) SSP (perspective view)   (e) WSP-A (perspective view)   (f) WSP-B (perspective view)

Fig. 9 Typical instantaneous three-dimensional near-wake structures of the smooth and wavy square prisms based on the Q-criteria detection. The iso-surface color indicates the streamwise velocity magnitude

5.3 Near-wake velocity distributions

Figs. 10 and 11 present time-averaged streamwise velocities ($\bar{u}$) and turbulent intensities (u_{rms}) distributions along the wake centerline, respectively. The smooth square prism case is included for a comparison purpose. In general, the LES data are in a good agreement with those from the present PIV measurement as well as the literature for both smooth and wavy square prisms. With increasing x/D_m $\bar{u}$ dips first and then increases rapidly after reaching a minimum, and finally approaches asymptotically a constant at $x/D_m > 6$ (Fig. 10). The minimum of $\bar{u}$ occurs at $x/D_m \approx$ 1.0−1.5 for both smooth and wavy square prisms. However, $\bar{u}$ -distributions for the wavy square prisms show distinguished behaviors at different spanwise locations. $\bar{u}$ for WSP-A exhibits a larger defect at the node than the saddle, suggesting a less entrainment of freestream flow into the near wake at the node plane. A different scenario is observed in the $\bar{u}$ -distributions for WSP-B (Fig. 10(c)); $\bar{u}$ has a larger defect at the saddle than the node. Comparatively, the minimum of $\bar{u}$ at the node for WSP-A is lower, compared to that at the saddle for WSP-B.
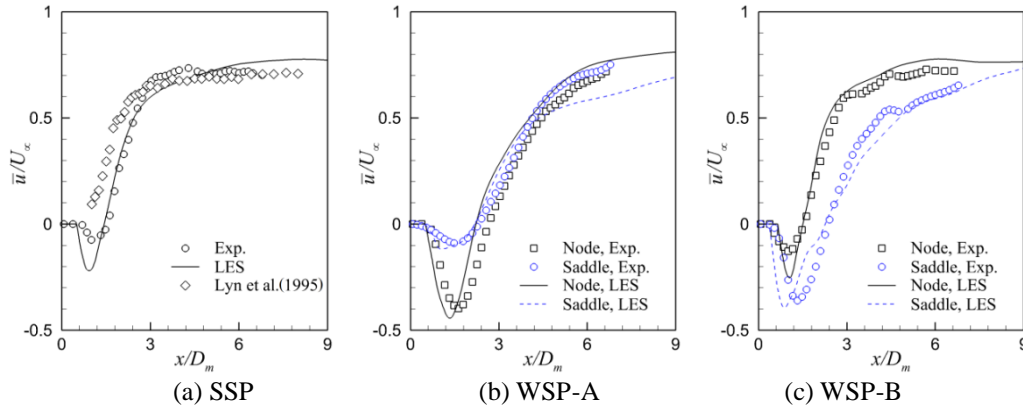

Fig. 10 Distributions of the time-averaged streamwise velocities along the wake centerline ($y = 0$) of the smooth and wavy square prisms
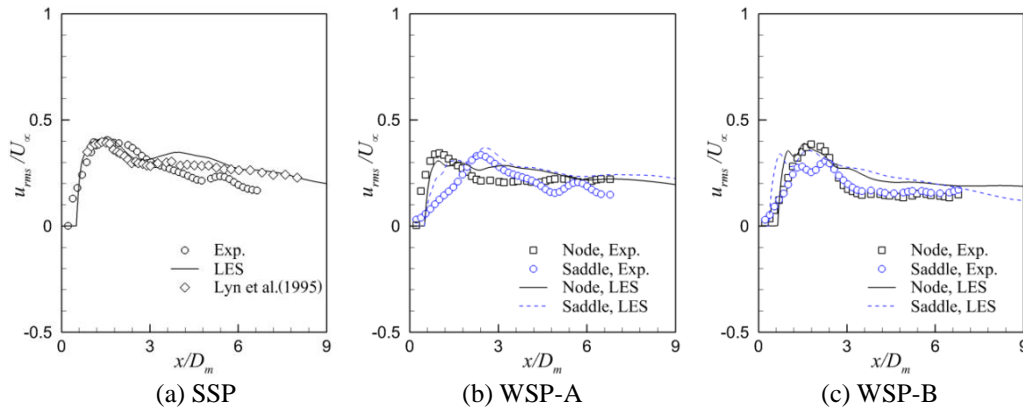

Fig. 11 Distributions of the turbulent intensities along the wake centerline ($y = 0$) of the smooth and wavy square prisms

Moreover, it can be seen that $\bar{u}$ distributions cross zero at different x/D_m for the smooth and wavy square prisms. The crossing occurs at $x/D_m \approx 1.5$ for the former (Fig. 10(a)), but at a larger x/D_m for the latter (Figs. 10(b) and 10(c)). For WSP-A, they cross zero at $x/D_m \approx 2.4$ at both node and saddle (Fig. 10(b)); however, for WSP-B, the crossing takes place at $x/D_m \approx 1.5$ and 2.4 at the node and saddle, respectively. It is well-known that the location of crossing zero in the $\bar{u}$ -distributions indicates the streamwise length of the recirculation bubble or vortex formation length (cf. Fig. 8). Hence, these observations indicate that the wavy square prisms have a longer vortex formation length in the near wake, particularly for WSP-A, than the smooth square prism, consistent with the observation in the time-averaged streamline patterns (Figs. 6 and 7).

In Fig. 11, u_{rms} increases rapidly and then declines gradually after reaching a maximum, with increasing x/D_m. The maximum of u_{rms} is detected approximately at the locations where the corresponding $\bar{u}$ distribution crosses zero, revealing the largest turbulent intensities at the edge of the wake bubble. Furthermore, the maxima for WSP-A at both node and saddle are lower than those for WSP-B as well as SSP, indicating reduced turbulent intensities in the near wake of WSP-A.

5.4 Vortex-shedding frequency and Strouhal number

Fig. 12 presents power spectra of the streamwise velocities in the near wake of the smooth and wavy square prisms. The abscissa is the normalized frequency ($f^* = fD_m/U_\infty$). Obviously, a pronounced peak is identified in the power spectrum for SSP or WSP-A or B, indicating the dominant shedding frequency (f_s) of vortices in the near wake, which is defined by the Strouhal number $St = f_s D_m/U_\infty$. The peak for WSP-A (Fig. 12(b)) is the weakest, consistent with the mostly suppressed fluctuating lift (Fig. 3(b) and Table 3). For SSP, the spectrum peak occurs at $St = 0.132$, in a good agreement with that in the literature. For WSP-A, one peak at $St = 0.121$ is detected at the node, while other two peaks at $St = 0.182$ and 0.101 are detected at the saddle. The occurrences of the lower $St = 0.121$ and the higher $St = 0.182$ for WSP-A than the $St = 0.132$ for SSP are partially ascribed to the larger and smaller bluff-heights of the prism at the corresponding locations.
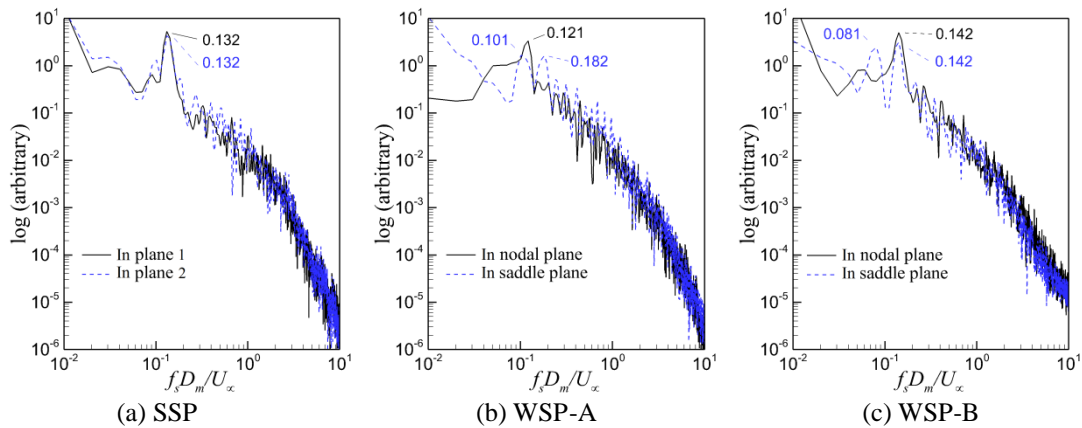

Fig. 12 Power spectra of the fluctuating streamwise velocities in the near wake of the smooth and wavy square prisms at $x/D_m = 2$ and $y/D_m = 0.5$

Though the saddle and node of WSP-A have the same amount (i.e., $0.15D_m$) of decrease and increase in the prism height with respect to the height of SSP, the modification of St from that of SSP is much larger at the saddle than the node. The lower $St = 0.101$ at the saddle is perhaps due to interactions between vortex shedding at $St = 0.121$ and 0.182. For WSP-B (Fig. 12(c)), the effect of the prism width on St is reversed, i.e., a higher $St = 0.142$ and a lower $St = 0.081$ are identified at the node and saddle, respectively, connected to a longer and a shorter afterbody length at the two planes, respectively. Again, the modification of St from that of SSP is greater at the saddle than the node.

6. Conclusions

The turbulent wake of a square prism with its faces modified into sinusoidal waves was investigated at $Re_{Dm} = 16,500$–$22,000$ using three-dimensional LES and PIV techniques. Modification of the side faces (WSP-A) and that of the front and rear faces (WSP-B) were adopted individually. The wavelength of the wavy faces for either case is $6D_m$ with an amplitude of $0.15D_m$. Compared with those of SSP, $\overline{C}_D$ and C'_L are respectively reduced by 8.7% and 78.2% for WSP-A and 2.4% and 32.1% for WSP-B, a maximum reduction occurring for WSP-A. WSP-A has a wide and a narrow wake at the node and saddle planes, respectively; the opposite scenario prevails for WSP-B, with the wide and narrow wakes swapping their correspondence to the planes. Consequently, there is a wide reversed flow region, associated with a long recirculation bubble or vortex formation length, in the near wake of WSP-A, corroborating the significant drag reduction and fluctuating lift suppression. Moreover, while the smooth prism corresponds to a single St, two distinct St were identified in the near wake of the wavy square prism, due to the three-dimensional alteration of the near wake by the sinusoidal variation of the faces. A lower and a higher St, compared to the St for SSP, correspond to the node and saddle, respectively, for WSP-A, whilst those communicate the saddle and node, respectively, for WSP-B.

Acknowledgments

References

Bearman, P.W. and Owen, J.C. (1998), "Reduction of bluff-body drag and suppression of vortex shedding by the introduction of wavy separation lines", *J. Fluid Struct.*, **12**(1), 123-130.
Bruno, L., Fransos, D., Coste, N. and Bosco, A. (2010), "3D flow around a rectangular cylinder: A computational study", *J. Wind Eng. Ind. Aerod.*, **98**(6-7), 263-276.
Choi, H.C., Jeon, W.P. and Kim, J.S. (2008), "Control of flow over a bluff body", *Annu. Rev. Fluid Mech.*, **40**, 113-139.
Darekar, R.M. and Sherwin, S.J. (2001), "Flow past a square-section cylinder with a wavy stagnation face",

J. Fluid Mech., **426**, 263-295.

Gu, Z.F. and Sun, T.F. (1999), "On interference between two circular cylinders in staggered arrangement at high subcritical Reynolds numbers", *J. Wind Eng. Ind. Aerod.*, **80**(3), 287-309.

Hunt, J.C.R., Wray, A.A. and Moin, P. (1998), "Eddies, streams, and convergence zones in turbulent flows", Center for Turbulence Research, Annu. Res. Briefs, 193-202.

Kuroda, M., Tamura, T. and Suzuki, M. (2007), "Applicability of LES to the turbulent wake of a rectangular cylinder - Comparison with PIV data", *J. Wind Eng. Ind. Aerod.*, **95**(9-11), 1242-1258.

Lam, K. and Lin, Y.F. (2008), "Large eddy simulation of flow around wavy cylinders at a subcritical Reynolds number", *Int. J. Heat Fluid Fl.*, **29**(4), 1071-1088.

Lam, K. and Lin, Y.F. (2009), "Effects of wavelength and amplitude of a wavy cylinder in cross-flow at low Reynolds numbers", *J. Fluid Mech.*, **620**, 195-220.

Lam, K., Lin, Y.F., Zou, L. and Liu, Y. (2010), "Experimental study and large eddy simulation of turbulent flow around tube bundles composed of wavy and circular cylinders", *Int. J. Heat Fluid Fl.*, **31**(1), 32-44.

Lam, K., Lin, Y.F., Zou, L. and Liu, Y. (2012), "Numerical study of flow patterns and force characteristics for square and rectangular cylinders with wavy surfaces", *J. Fluid Struct.*, **28**, 359-377.

Lam, K., Wang, F.H. and So, R.M.C. (2004), "Three-dimensional nature of vortices in the near wake of a wavy cylinder", *J. Fluid Struct.*, **19**(6), 815-833.

Liang, C. and Papadakis, G. (2007), "Large eddy simulation of pulsating flow over a circular cylinder at subcritical Reynolds number", *Comput. Fluids*, **36**(2), 299-312.

Lyn, D.A., Einav, S., Rodi, W. and Park, J.H. (1995), "A laser-Doppler velocimetry study of ensemble-averaged characteristics of the turbulent near wake of a square cylinder", *J. Fluid Mech.*, **304**, 285-319.

Mankbadi, M.R. and Georgiadis, N.J. (2015), "Examination of parameters affecting large-eddy simulation of flow past a square cylinder", *AIAA J.*, **53**(6), 1706-1712.

Mannini, C., Soda, A. and Schewe, G. (2010), "Unsteady RANS modelling of flow past a rectangular cylinder: Investigation of Reynolds number effects", *Comput. Fluids*, **39**(9), 1609-1624.

New, T.H., Shi, S. and Liu, Y. (2013), "Cylinder-wall interference effects on finite-length wavy cylinders at subcritical Reynolds number flows", *Exp. Fluids*, **54**(10), 1601.

New, T.H., Shi, S. and Liu, Y. (2015), "On the flow behaviour of confined finite-length wavy cylinders", *J. Fluid Struct.*, **54**, 281-296.

Noda, H. and Nakayama, A. (2003), "Reproducibility of flow past two-dimensional rectangular cylinders in a homogeneous turbulent flow by LES", *J. Wind Eng. Ind. Aerod.*, **91**(1-2), 265-278.

Norberg, C. (1993), "Flow around rectangular cylinders: pressure forces and wake frequencies", *J. Wind Eng. Ind. Aerod.*, **49**(1-3), 187-196.

Oka, S. and Ishihara, T. (2009), "Numerical study of aerodynamic characteristics of a square prism in a uniform flow", *J. Wind Eng. Ind. Aerod.*, **97**(11-12), 548-559.

Smagorinsky, J. (1963), "General circulation experiments with the primitive equations. I. The basic experiment", *Mon. Weather Rev.*, **91**, 99-164.

Sohankar, A. (2008), "Large eddy simulation of flow past rectangular-section cylinders: Side ratio effects", *J. Wind Eng. Ind. Aerod.*, **96**(5), 640-655.